

# A Low-Voltage and High-Current Inductive Power Transfer System With Low Harmonics for Automatic Guided Vehicles

Fei Lu <sup>1</sup>, Member, IEEE, Yiming Zhang, Member, IEEE, Hua Zhang <sup>2</sup>, Member, IEEE, Chong Zhu <sup>3</sup>, Member, IEEE, Lijun Diao <sup>4</sup>, Senior Member, IEEE, Minming Gong, Weige Zhang, and Chris Mi <sup>5</sup>, Fellow, IEEE

**Abstract**—This paper proposes the series-series compensation topology to realize a low-voltage and high-current inductive power transfer system (IPT) for the automatic guided vehicles (AGVs). Since the height of the AGV chassis is in the tens of mm, the coupling coefficient is close to 1, resulting in a tightly coupled IPT system. This paper has three main contributions. First, it reveals that the high-order harmonic currents in a tightly coupled IPT system could be very significant. Second, it quantifies the impact of the high-order harmonic currents on the efficiency, which shows the efficiency can be reduced. Third, it proposes an effective method to design the parameters in order to reduce the harmonics and maintain high efficiency. Aiming at the charging of AGVs, a prototype is constructed. The magnetic coupler size is 220 mm × 220 mm × 10 mm. When the airgap is 10 mm, it achieves 1.8-kW power transfer with a dc-dc efficiency of 89.9% from a 400-V dc source to a 24-V dc load, and the charging current is 74 A. When the airgap varies from 5 mm to 15 mm, the power variation is within ±350 W, and the efficiency is not affected. The fast Fourier transform analysis of the experimental currents also validates the theoretical analysis and the simulation results.

**Index Terms**—Tightly-coupled, automatic guided vehicle (AGV), high-order harmonic, series-series compensation.

## NOMENCLATURE

|               |                       |
|---------------|-----------------------|
| $S_1$ – $S_4$ | Inverter MOSFETs.     |
| $L_1$         | Primary inductor.     |
| $k$           | Coupling coefficient. |
| $C_1$         | Primary capacitor.    |
| $f_{sw}$      | Switching frequency.  |
| $V_{in}$      | DC supply.            |
| $V_1$         | Input ac voltage.     |
| $I_1$         | Input ac current.     |

Manuscript received February 25, 2018; revised June 16, 2018, August 9, 2018, and October 19, 2018; accepted January 16, 2019. Date of publication February 11, 2019; date of current version April 16, 2019. This paper is funded by the US Department of Energy and was supported by Beijing Municipal Science & Technology Commission No. Z181100004418005. The review of this paper was coordinated by Prof. A. Rathore. (Corresponding author: Chris Mi.)

F. Lu and H. Zhang are with the Department of Electrical and Computer Engineering, Drexel University, Philadelphia, PA 19104 USA (e-mail: fei.lu@drexel.edu; hua.zhang@drexel.edu).

Y. Zhang, C. Zhu, and C. Mi are with the Department of Electrical and Computer Engineering, San Diego State University, San Diego, CA 92182 USA (e-mail: yiming.zhang@sdsu.edu; chong.zhu@sdsu.edu; cmi@sdsu.edu).

L. Diao, M. Gong, and W. Zhang are with the School of Electrical Engineering, Beijing Jiaotong University, Beijing 100044, China (e-mail: ljiao@bjtu.edu.cn; mmgong@bjtu.edu.cn; zhangwg@dq.njtu.edu.cn).

Digital Object Identifier 10.1109/TVT.2019.2898418

|                      |  |
|----------------------|--|
| $V_{1,n}$            | $n$ th harmonic of $V_1$ .                             |
| $I_{1,n}$            | $n$ th harmonic of $I_1$ .                             |
| $n$                  | Number of harmonic.                                    |
| $\theta$             | Phase difference between $V_1$ and $V_2$ .             |
| $Z_{inp}, Z_{ins}$   | Primary/secondary input impedance.                     |
| $Z_{Mp}, Z_{Ms}$     | Primary/secondary mutual impedance.                    |
| $I_{1p}, I_{2p}$     | Input/output current excited by primary source.        |
| $I_{1s}, I_{2s}$     | Input/Output current excited by secondary source.      |
| $k_n$                | Singular coupling coefficient to maximize harmonics.   |
| $A, B$               | Constant to calculate $I_{2s}$ .                       |
| $I_p$                | Primary current related to the self-inductance.        |
| $I_{pM}$             | Primary current related to the mutual inductance.      |
| $I_s$                | Secondary current related to the self-inductance.      |
| $I_{sM}$             | Secondary current related to the mutual inductance.    |
| $r_I$                | Current ratio related to primary/secondary parameters. |
| $P_1$                | Fundamental power.                                     |
| $P_{out}$            | Total power.   |
| $P_{cond}$           | Conductive loss.                                       |
| $N_p, N_s$           | Turn number of coils.                                  |
| $C_m, \alpha, \beta$ | Constant to calculate magnetic power loss.             |
| $D_1$ – $D_4$        | Rectifier diodes.                                      |
| $L_2$                | Secondary inductor.                                    |
| $L_M$                | Mutual inductance.                                     |
| $C_2$                | Secondary capacitor.                                   |
| $\omega_0$           | Angular frequency.                                     |
| $V_{out}$            | Battery voltage.                                       |
| $V_2$                | Output ac voltage.                                     |
| $I_2$                | Output ac current.                                     |
| $V_{2,n}$            | $n$ th harmonic of $V_2$ .                             |
| $I_{2,n}$            | $n$ th harmonic of $I_2$ .                             |
| $Q$                  | Quality factor.  |
| $P_n$                | Harmonic power.  |
| $P_{loss}$           | Power loss.  |
| $P_{mag}$            | Magnetic loss.   |
| $N_t$                | Turn ratio of coils.                                   |

## I. INTRODUCTION

THE inductive power transfer (IPT) technology can provide significant conveniences to charge electric vehicles [1],

[2]. The transfer distance is the height of the vehicle chassis, which is typically in the hundreds of mm for a passenger car, and the coupling coefficient between the transmitter and receiver is usually below 0.30, resulting in a loosely-coupled IPT system [3], [4]. Therefore, a compensation circuit is required on both sides to resonate with the coils and increase the power transfer capability [5]–[7]. In previous research, different compensation topologies, such as series, parallel, LCL, and LCC, have been proposed and studied [8], [9].

The series-series (SS) compensation has been widely used due to its simplicity [10]. There is only one capacitor at each side, which reduces the system size and cost. The working principle and frequency property have been well investigated. If the self-inductance is compensated, it works as a current source to charge the battery [11]. Further studies also show a good load-independent performance, which means the charging current is immune to the variation of battery voltage [12], [13]. During the entire charging process, the equivalent load resistance varies with the charging power [14], and the circuit parameters can be optimized to achieve a relatively high efficiency [15], [16]. Also, since the relative position between the transmitter and receiver changes in a dynamic system [17], the system power is affected. Therefore, some studies attempt to maintain stable transfer power through the system structure and control strategy design [18], [19]. In addition, a current-fed half-bridge configuration can be further applied to improve the performance, in which the current stress on the voltage source inverter (VSI) is reduced and the light load instability is mitigated [20].

When an IPT system is applied to charge an automatic guided vehicle (AGV), it has two benefits. First, the size of the on-board battery pack can be reduced. Second, since the AGV can be charged in the loading and unloading status, the effective working time can be significantly increased [21]–[23]. However, the height of the AGV chassis is usually in the tens of mm, and it can even decrease to a few mm in the full-loading condition [24]–[26]. This short distance between the transmitter and receiver can lead to a coupling coefficient close to 1.0, resulting in a tightly-coupled IPT system. In this scenario, the coupling coefficient is also sensitive to the airgap variation. Moreover, the battery voltage on an AGV is usually 24 V due to the safety requirement, but the current should be high to reduce the charging time. Therefore, the low-voltage and high-current working condition introduces extra difficulties in designing an IPT system for the charging of AGVs.

Typically, there are three possible solutions to achieve a tightly-coupled IPT system for AGV charging: LLC converter [27], SS compensation, and LCC compensation [5]. The LLC converter can eliminate the receiver side capacitor. However, it works as a voltage source and requires precise frequency tuning during the charging process, which increases the system complexity. Moreover, when there is airgap variation, the charging current can be dramatically changed, which is difficult to use in a real system. The double-sided LCC compensation can achieve a constant current, but the AGV side space cannot support so many bulky passive components.

Therefore, this paper proposes to apply the SS circuit in this design. Its simple structure can reduce the system cost. When the

self-inductance is compensated, the circuit works as a constant-current source, and the charging current can be easily controlled by tuning the input-side voltage, which is convenient for the practical implementation. In the study of the SS compensated IPT system for the AGV charging application, the paper has three main contributions.

First, this paper reveals that there is a large amount of high-order harmonic currents in a tightly-coupled SS compensated IPT system. The theoretical calculation shows that when the coupling coefficient is close to 1.0, the high-order harmonic currents becomes very significant.

Second, this paper quantifies the impact of the high-order harmonic currents on the efficiency of the tightly-coupled IPT system. In the previous study of the loosely-coupled IPT system, increasing the coupling coefficient helps increase the efficiency. However, the tightly-coupled system is different. This paper shows that the efficiency is reduced by the harmonic currents in a tightly-coupled system.

Third, this paper proposes an effective method to design the circuit parameters, which can solve the problems of high-order harmonic currents and the efficiency drop. A parameter  $r_I$  is proposed as the guideline to design the circuit parameters. The experimental results validate that the current distortion is limited and the high-efficiency working status is realized.

The previous study on harmonics in an IPT system mainly focuses on the loosely-coupled IPT system. The waveform distortion is small in the full-load scenario, and the distortion of the current only occurs in the light-load condition [28]–[30]. In order to reduce the harmonics, there are mainly three methods. First, an additional low-pass filter is added in the circuit [30], and the cost and weight are increased. Second, a multi-level inverter is used to eliminate the high-order harmonics from the input excitation side, and extra hardware circuit is required, which also increases the system complexity [31]. Third, the phase-shift control is used in the inverter to eliminate the selective order of harmonics [32]–[34], but this method cannot make full use of the input-side dc bus voltage. Since the third-order harmonic is difficult to be fully-eliminated, it can be used to transfer power instead, and the circuit is designed to resonate at the third-order frequency [35]–[37]. In some other applications, this design can also support multiple receivers at the fundamental and third-order frequency, respectively [38].

Different from the conventional loosely-coupled IPT system, one distinguishing challenge of a tightly-coupled IPT system is that the high-order harmonics occur in both full- and light-load conditions. Moreover, in a loosely-coupled IPT system, the maximum THD is usually lower than 30%. However, this paper shows that the maximum THD of a tightly-coupled IPT system can exceed 200% if the parameters are not well designed. Therefore, it is more meaningful to study the harmonics in a tightly-coupled IPT system. In addition, since the THD of a loosely-coupled IPT system is relatively small, the influence on the efficiency and power is negligible and the studies in [39] and [40] are reasonable. As an improvement to the previous work, this paper shows that the efficiency and power analysis need to be amended due to the large amount of harmonics in a tightly-coupled IPT system.

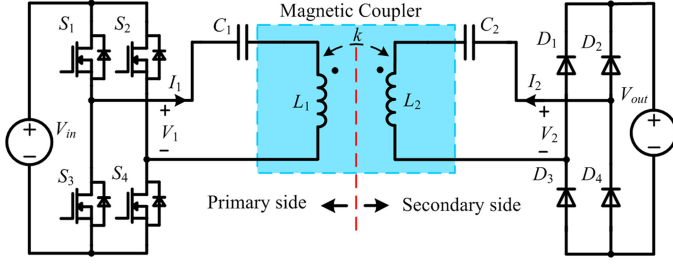


Fig. 1. Circuit topology of an SS-compensated IPT system.

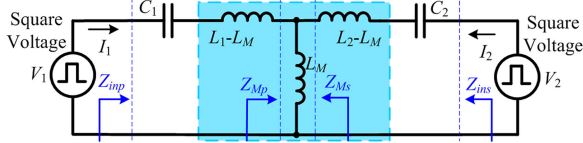


Fig. 2. Simplified circuit topology of an SS-compensated IPT system.

## II. HIGH-ORDER HARMONIC ANALYSIS

### A. Circuit Working Principle

The circuit topology of an SS-compensated IPT system is shown in Fig. 1. The parameter relationship is shown below.

$$\begin{cases} L_M = k \cdot \sqrt{L_1 L_2} \\ \omega_0 = 1/\sqrt{L_1 C_1} = 1/\sqrt{L_2 C_2} \end{cases} \quad (1)$$

The mutual inductance is defined as  $L_M$ , and the resonant angular frequency is defined as  $\omega_0$ . To analyze its working principle, the circuit is simplified in Fig. 2. The magnetic coupler is represented by a T model. Two square-wave sources  $V_1$  and  $V_2$  are used to represent the excitations, and the phase difference between  $V_1$  and  $V_2$  is defined as  $\theta$ . If  $V_2$  is set as the reference phasor, the voltages  $V_1$  and  $V_2$  are expressed as in (2).

$$\begin{cases} V_1 = |V_{in}| \cdot 4/\pi \cdot [\sin(\omega_0 t + \theta) + \sin(3\omega_0 t + 3\theta)/3 + \dots] \\ \quad = \sum_{n=1,3,\dots}^{\infty} (V_{1,n}) \\ V_2 = |V_{out}| \cdot 4/\pi \cdot [\sin(\omega_0 t) + \sin(3\omega_0 t)/3 + \dots] \\ \quad = \sum_{n=1,3,\dots}^{\infty} (V_{2,n}) \end{cases} \quad (2)$$

It shows that  $V_1$  and  $V_2$  both contain the fundamental and high-order harmonics. The magnitudes of the fundamental parts are specified as  $|V_{1,1}| = 4/\pi \times |V_{in}|$  and  $|V_{2,1}| = 4/\pi \times |V_{out}|$ . Then, the superposition theory is used to analyze the circuit.

When the resonant circuit is excited only by  $V_1$ , the primary and secondary currents induced by  $V_1$  are defined as  $I_{1p}$  and  $I_{2p}$ . At the high-order harmonic frequency  $\omega_n = n\omega_0$  ( $n = 3, 5, 7, \dots$ ), two equivalent impedances  $Z_{inp}$  and  $Z_{Mp}$

are defined in Fig. 2, and expressed as (3) shown at the bottom this page.

When only  $V_1$  is excited, according to Fig. 2, the currents  $I_{1p}$  and  $I_{2p}$  are further calculated as

$$\begin{cases} I_{1p} = V_1 / Z_{inp} \\ I_{2p} = -I_{1p} \cdot Z_{Mp} / [j\omega_0(L_2 - L_M) + 1/(j\omega_0 C_2)] \end{cases} \quad (4)$$

By substituting (3) shown at the bottom of this page, into (4),  $I_{1p}$  and  $I_{2p}$  are further calculated as in (5). Both the fundamental and high-order frequencies are considered. Different frequency components can be analyzed separately. Since this is a linear circuit, the results can be added to get the expressions of  $I_{1p}$  and  $I_{2p}$ .

$$\begin{cases} I_{1p} = \sum_{n=3,5,\dots}^{\infty} V_{1,n} \\ \quad \cdot (1 - 1/n^2) / [j\omega_0 L_1 \cdot n \cdot ((1 - 1/n^2)^2 - k^2)] \\ I_{2p} = V_{1,1} / (j\omega_0 L_M) \\ \quad - \sum_{n=3,5,\dots}^{\infty} V_{1,n} k^2 / [j\omega_0 L_M n \cdot ((1 - 1/n^2)^2 - k^2)] \end{cases} \quad (5)$$

It shows that  $I_{1p}$  only contains the high-order harmonics, and  $I_{2p}$  contains both fundamental and high-order components.

When the resonant circuit is excited only by  $V_2$ , the primary and secondary induced currents are defined as  $I_{1s}$  and  $I_{2s}$ . Two equivalent impedances  $Z_{ins}$  and  $Z_{Ms}$  are also defined as in Fig. 2. Then, from the circuit, the currents  $I_{1s}$  and  $I_{2s}$  are calculated as

$$\begin{cases} I_{2s} = V_2 / Z_{ins} \\ I_{1s} = -I_{2s} \cdot Z_{Ms} / [j\omega(L_1 - L_M) + 1/(j\omega C_1)] \end{cases} \quad (6)$$

Similarly, by substituting  $V_2$ ,  $Z_{Ms}$ , and  $Z_{ins}$  into (6),  $I_{1s}$  and  $I_{2s}$  are calculated at both fundamental and high-order frequencies

$$\begin{cases} I_{1s} = V_{2,1} / (j\omega_0 L_M) \\ \quad - \sum_{n=3,5,\dots}^{\infty} V_{2,n} k^2 / [j\omega_0 L_M n \cdot ((1 - 1/n^2)^2 - k^2)] \\ I_{2s} = \sum_{n=3,5,\dots}^{\infty} V_{2,n} \\ \quad \cdot (1 - 1/n^2) / [j\omega_0 L_2 \cdot n \cdot ((1 - 1/n^2)^2 - k^2)] \end{cases} \quad (7)$$

It shows that  $I_{2s}$  only contains high-order harmonics, and  $I_{1s}$  contains both fundamental and high-order components.

### B. Analysis of Phase Difference $\theta$ Between $V_1$ and $V_2$

According to the superposition theorem, the currents excited by the two sources can be added together, resulting in  $I_1$  and  $I_2$  as shown in Fig. 2. Then, in the time domain,  $I_1(t)$  and  $I_2(t)$  are calculated as in (8). It means that each current relates to both

$$\begin{cases} Z_{Mp} = j\omega_0 L_M n [(1 - 1/n^2) - k^2 L_1 / L_M] / (1 - 1/n^2) \\ Z_{inp} = j\omega_0 L_1 \cdot n \cdot [(1 - 1/n^2)^2 - k^2] / (1 - 1/n^2) \end{cases}, n = 3, 5, 7, \dots \quad (3)$$

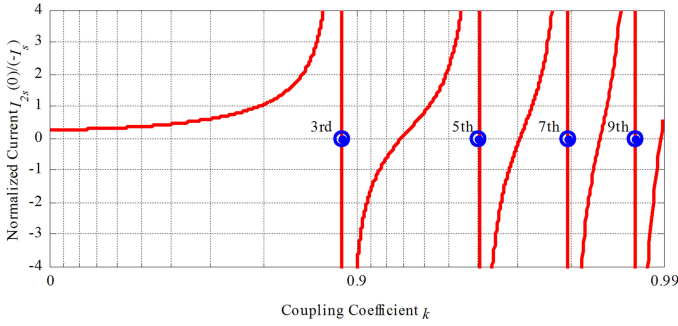


Fig. 3. Normalized current  $I_{2s}(0)/(-I_s)$  at different coupling coefficient  $k$ .

voltage sources.

$$\begin{cases} I_1(t) = I_{1p}(t) + I_{1s}(t) \\ I_2(t) = I_{2p}(t) + I_{2s}(t) \end{cases} \quad (8)$$

In the secondary rectifier, the diodes commute when the current  $I_2$  changes direction. Therefore, the secondary current  $I_2$  should be zero when the voltage  $V_2$  is zero, which means

$$I_2(0) = 0 = I_{2p}(0) + I_{2s}(0) \quad (9)$$

This relationship between  $I_{2p}(0)$  and  $I_{2s}(0)$  will be used to derive the phase angle  $\theta$  between the two voltage sources.

First, we can look at  $I_{2s}(0)$ . According to (7), when  $t = 0$ , the current  $I_{2s}(0)$  can be calculated and simplified as

$$\begin{aligned} I_{2s}(0) &= -|V_{2,1}| / (\omega_0 L_2) \\ &\times \sum_{n=3,5,\dots}^{\infty} (n^2 - 1) / \left( (n^2 - 1)^2 - n^4 k^2 \right) \\ &= -I_s / 2 \\ &\cdot \sum_{n=3,5,\dots}^{\infty} \left( 1 / (n^2(1 - k) - 1) + 1 / (n^2(1 + k) - 1) \right) \\ &= -I_s \pi / 8 [A (\cot(A\pi/2) - 2 \cot(A\pi)) \\ &\quad + B (\cot(B\pi/2) - 2 \cot(B\pi))] \end{aligned} \quad (10)$$

where  $I_s$ ,  $A$ , and  $B$  are defined as

$$I_s = |V_{2,1}| / (\omega_0 L_2), A = 1/\sqrt{1-k}, B = 1/\sqrt{1+k} \quad (11)$$

Therefore, for a given coupling coefficient  $k$ , the current  $I_{2s}(0)$  can be calculated using (10) and (11). Then, the normalized  $I_{2s}(0)$  with respect to  $(-I_s)$  is shown in Fig. 3.

Fig. 3 shows that, in a loosely-coupled IPT system when  $k$  is much smaller than  $8/9$ , the normalized current increases with  $k$ . However, in a tightly-coupled IPT system when  $k$  is close to  $1.0$ , the singular working condition for the high-order harmonic is

$$k_n = 1 - 1/n^2, n = 3, 5, 7, \dots \quad (12)$$

At the singular coupling coefficient  $k_n$ , the magnitude of the current  $I_{2s}(0)$  is approaching infinity, which is an unstable working condition we should avoid.

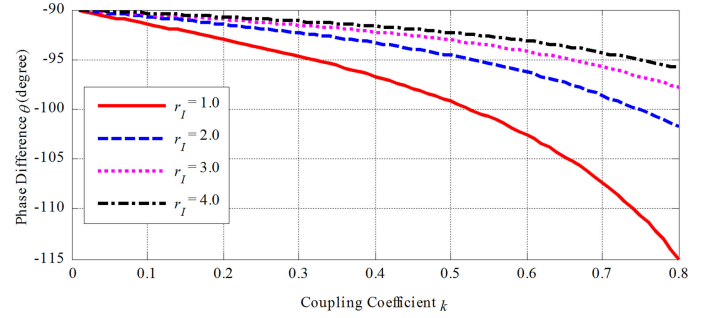


Fig. 4. Phase difference  $\theta$  between  $V_1$  and  $V_2$  at different values of  $r_I$  and  $k$ .

Second, we can look at  $I_{2p}(0)$ . According to (5), when  $t = 0$ ,  $I_{2p}(0)$  is calculated as

$$I_{2p}(0) = \frac{I_{pM}}{k} \left( \sin(\theta - 90^\circ) - \sum_{n=3,5,\dots}^{\infty} \frac{n^2 k^2 \sin(n\theta - 90^\circ)}{(n^2 - 1)^2 - n^4 k^2} \right) \quad (13)$$

where,  $I_{pM}$  is defined as

$$I_{pM} = |V_{1,1}| / \left( \omega_0 \sqrt{L_1 L_2} \right) \quad (14)$$

Similarly, (13) also shows the same singular coupling coefficient  $k_n$  as in (12). At the singular conditions, there are significant high-order harmonic currents as indicated in (10) and (13). In addition, the singular conditions are close to each other, meaning the system is sensitive to parameter variations. Therefore, a practical IPT system should avoid working around the singular range.

Therefore, according to (9), (10), and (13), the phase difference  $\theta$  between  $V_1$  and  $V_2$  is calculated. In the calculation process, a parameter  $r_I$  is proposed and defined as the in-out ratio, which is expressed in (15).

$$r_I = \frac{I_{pM}}{I_s} = \frac{|V_{1,1}|}{|V_{2,1}|} \cdot \frac{\sqrt{L_2}}{\sqrt{L_1}} \quad (15)$$

This in-out ratio  $r_I$  represents the relationship between the input and output voltages, and also the relationship between the input and output self-inductances. It is used as the guideline to design the circuit parameters of a tightly-coupled IPT system.

Then,  $\theta$  is expressed at different  $r_I$  and  $k$  in Fig. 4. It shows that  $\theta$  increases with an increasing  $k$  and a decreasing  $r_I$ . In a loosely-coupled IPT system with a relative low  $k$ ,  $\theta$  is close to  $-90^\circ$ . However, in a tightly-coupled IPT system, when  $k$  is approaching  $0.80$ ,  $\theta$  can be even lower than  $-115^\circ$ .

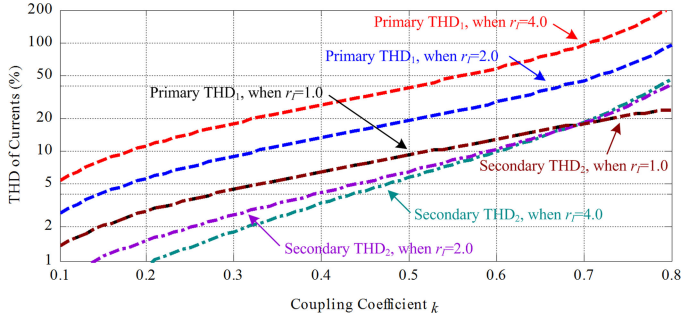
### C. Calculation of the High-Order Harmonic Currents

Based on the phase difference  $\theta$ , the fundamental currents  $I_{1,1}$  and  $I_{2,1}$  at the input and output sides are expressed as

$$\begin{cases} I_{1,1} = I_{sM}/k \cdot \sin(\omega_0 t - 90^\circ) \\ I_{2,1} = I_{pM}/k \cdot \sin(\omega_0 t + \theta - 90^\circ) \end{cases} \quad (16)$$

where,  $I_p$  and  $I_{sM}$  are defined as

$$I_p = |V_{1,1}| / (\omega_0 L_1), I_{sM} = |V_{2,1}| / \left( \omega_0 \sqrt{L_1 L_2} \right) \quad (17)$$


 Fig. 5. Total harmonic distortion (THD) at different values of  $r_I$  and  $k$ .

Also, the  $n$ th ( $n = 3, 5, 7, \dots$ ) high-order harmonic current is

$$\begin{cases} I_{1,n}(t) = I_p (n^2 - 1) \\ \cdot \sin(n\omega_0 t + n\theta - 90^\circ) / [(n^2 - 1)^2 - n^4 k^2] \\ - I_{sM} k \cdot n^2 \cdot \sin(n\omega_0 t - 90^\circ) / [(n^2 - 1)^2 - n^4 k^2] \\ I_{2,n}(t) = -I_{pM} k \cdot n^2 \\ \cdot \sin(n\omega_0 t + n\theta - 90^\circ) / [(n^2 - 1)^2 - n^4 k^2] \\ + I_s (n^2 - 1) \cdot \sin(n\omega_0 t - 90^\circ) / [(n^2 - 1)^2 - n^4 k^2] \end{cases} \quad (18)$$

The total harmonic distortion (THD) of the primary and secondary currents  $I_1$  and  $I_2$  are defined as

$$\begin{aligned} THD_1 &= \sqrt{\sum_{n=3,5,\dots}^{\infty} |I_{1,n}|^2} / |I_{1,1}|, THD_2 \\ &= \sqrt{\sum_{n=3,5,\dots}^{\infty} |I_{2,n}|^2} / |I_{2,1}| \end{aligned} \quad (19)$$

Therefore, based on the fundamental and harmonic currents in (16) and (18), the current distortion is shown in Fig. 5. It shows that the THD increases with  $k$ , which means a tightly-coupled IPT system generates more harmonics than a loosely-coupled system. When the ratio  $r_I$  increases, the primary current THD increases to an extremely large value, which needs to be avoided. To clarify, the calculation also shows that the third-order harmonic dominate the distortion.

#### D. System Power and Efficiency Analysis

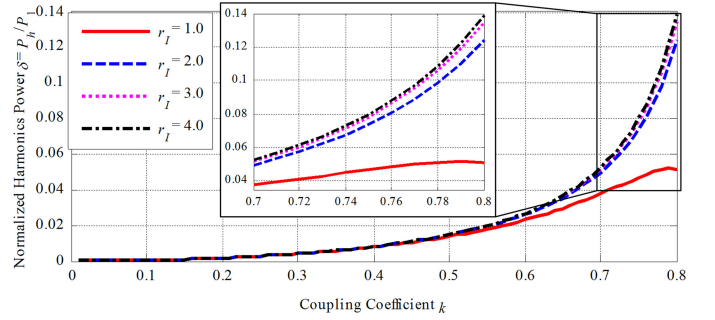
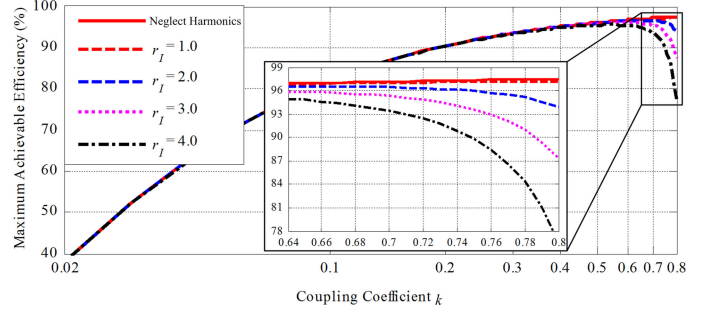
At the fundamental frequency  $\omega_0$ , the system power is

$$P_1 = |V_{1,1}| \cdot |V_{2,1}| / (2\omega_0 L_M) \cdot \sin(-\theta) \quad (20)$$

It shows the relationship between the fundamental power  $P_1$  and the circuit parameters. For the high-order harmonics, the harmonic power  $P_n$  is calculated as

$$\begin{aligned} P_n &= |V_{1,1}| |V_{2,1}| / (2\omega_0 L_M) \cdot k^2 n / [(n^2 - 1)^2 - n^4 k^2] \\ &\cdot \sin(n\theta), n = 3, 5, \dots \end{aligned} \quad (21)$$

It shows that the harmonic power relates to its order number  $n$ . Then, the total harmonic power is defined as  $P_h$ , and the


 Fig. 6. Normalized total harmonic power  $\delta$  at different values of  $r_I$  and  $k$ .

 Fig. 7. Maximum achievable efficiency of an SS-compensated IPT system when  $Q = 100$ , considering high-order harmonic currents.

system output power  $P_{out}$  can be expressed as

$$\begin{aligned} P_{out} &= P_1 + \sum_{n=3,5,\dots}^{\infty} P_n = P_1 + P_h = P_1 \cdot (1 + \delta), \\ \delta &= P_h / P_1 \end{aligned} \quad (22)$$

Based on the calculated phase difference  $\theta$  in Fig. 4, and the THD in Fig. 5, the normalized total harmonic power  $\delta$  is calculated as shown in Fig. 6.

It shows that  $P_h$  increases with the increasing  $r_I$  and  $k$ , which means the high-order harmonic currents contribute to power transfer. However, it also shows this contribution is limited. For example, when  $r_I = 4.0$  and  $k = 0.8$ , the harmonic power  $P_h$  is only about 14% of the fundamental power  $P_1$ .

In an IPT system, the power loss  $P_{loss}$  consists of conductive loss  $P_{cond}$  and magnetic loss  $P_{mag}$  [41]. The magnetic loss  $P_{mag}$  can be expressed by the Steinmetz equation as

$$P_{mag} = C_m f_{sw}^\alpha B^\beta \quad (23)$$

where  $B$  is the magnetic field density, and  $C_m$ ,  $\alpha$ , and  $\beta$  are three coefficients related to the magnetic material. For example, these values are  $C_m = 2.08 \times 10^{-6}$ ,  $\alpha = 1.43$ ,  $\beta = 2.41$  for PC40. When only the fundamental current is considered, the maximum efficiency is analyzed in [2], [39] and [40]. However, when the high-order harmonics are considered, the efficiency reduces. Therefore, based on Fig. 5, the maximum achievable efficiency of an SS-compensated system is shown in Fig. 7, where the quality factor  $Q$  of the resonant circuit is 100 as an example.

Fig. 7 shows that, if the high-order harmonic currents are neglected, the system efficiency keeps increasing with  $k$ . It is

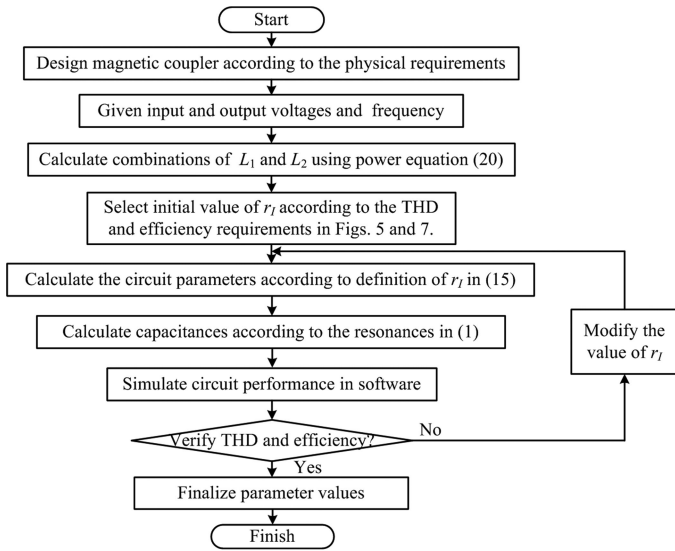


Fig. 8. Design procedure of a tightly-coupled IPT system considering the THD and efficiency.

true in a loosely-coupled IPT system, because the high-order harmonics are small. However, in a tightly-coupled IPT system, it is different. With relatively large  $k$  and  $r_I$ , the high-order harmonics are significant and the efficiency is decreased. For example, when  $r_I = 4.0$  and  $k = 0.8$ , the THD of the  $I_1$  is 200%, and the efficiency reduces to 78%. Then, in a tightly-coupled IPT system, parameters should be designed properly to reduce the high-order harmonics and maintain the high efficiency.

## II. A DESIGN EXAMPLE OF AGV CHARGING

### A. Discussion on Parameter Design Method

According to the above analysis, it shows that the system performance closely relates to the coupling coefficient  $k$  and the in-out ratio  $r_I$ . Usually, the system design target is to reduce the THD and improve the efficiency. For the coupling coefficient  $k$ , it is very high in a tightly-coupled system that can cause harmonics. For the in-out ratio  $r_I$ , it is used to reduce the harmonics and maintain the system efficiency. Based on its definition,  $r_I$  relates to two kinds of parameters: the external ones (input and output voltages  $V_1$  and  $V_2$ ) and the internal ones (input and output inductances  $L_1$  and  $L_2$ ). According to (15), when the input and output voltages are given, increasing the primary inductance  $L_1$  is the key to reduce harmonics.

The step-by-step design procedure of a tightly-coupled IPT system is shown in Fig. 8. First, the magnetic coupler is designed according to the physical requirements, providing the coupling coefficient and the single-turn inductance value. Second, with the given input and output voltages and the switching frequency, the product of  $L_1$  and  $L_2$  can be calculated using the power equation (20). Then, according to the THD and efficiency requirements in Figs. 5 and 7, a proper initial value of  $r_I$  is selected. Third, the inductance  $L_1$  and  $L_2$  can be further determined using the definition of  $r_I$  in (15). Also, the compensation capacitances are calculated using (1). Fourth, the circuit performance is simulated. If both the THD and efficiency satisfy

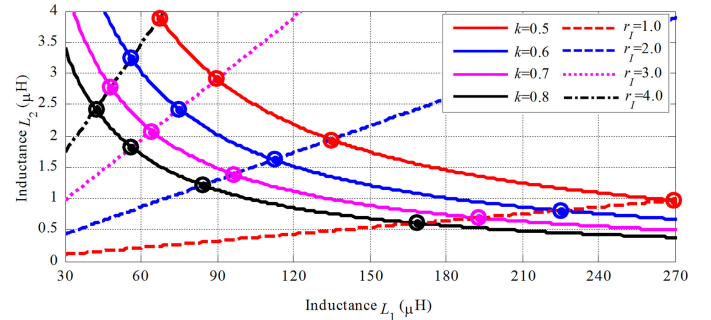


Fig. 9. Inductance  $L_1$  and  $L_2$  at different values of  $k$  and  $r_I$  in a 1.8 kW IPT system when  $V_{in} = 400$  V and  $V_{out} = 24$  V.

the requirements, we can finalize the parameters and finish the process. If not, we need to modify  $r_I$  (usually, reduce its value), and repeat the third step until both the THD and efficiency requirements are satisfied.

### B. AGV Charging Example Design

A low-voltage and high-current IPT system is designed for the AGV charging using the proposed design method above. The input dc voltage  $V_{in}$  is 400 V, and the battery voltage  $V_{out}$  is only 24 V. From (17),  $L_1$  and  $L_2$  are calculated at different values of  $k$  as the solid lines in Fig. 9. Then, according to (12),  $L_1$  and  $L_2$  can also be calculated at different values of  $r_I$  as the dashed lines in Fig. 9.

In Fig. 9, the system power is maintained at 1.8 kW for different values of  $k$ . The special combinations of  $L_1$  and  $L_2$  are labeled as the cross points at different values of  $k$  and  $r_I$ . When  $k$  increases,  $L_1$  and  $L_2$  trend to decrease. For a specific value of  $k$ , increasing  $L_1$  helps to reduce  $r_I$ . According to Section II, the decrease of  $r_I$  can reduce high-order harmonics and maintain high efficiency.

### C. Circuit Performance Simulation

Based on the combinations of  $L_1$  and  $L_2$  in Fig. 9, the system performance is simulated in LTspice. The switching frequency is 85 kHz and. When  $r_I = 1.0$ , the simulated waveforms of  $I_1$  and  $(-I_2)$  at different values of  $k$  are shown in Fig. 10. It shows that both  $I_1$  and  $(-I_2)$  are distorted when  $k$  increases, which agrees with the calculation results Fig. 5.

According to the simulations, the circuit parameters should be designed to limit  $r_I$  and  $k$ , which is the guideline in designing an IPT system. Therefore, in an AGV charging application,  $k$  is designed to be around 0.70 and  $r_I$  is designed to be around 1.0, resulting in the parameters as shown in Table I.

## III. EXPERIMENTAL VALIDATION

### A. Prototype Implementation

According to Table I, a prototype of a tightly-coupled IPT system is implemented as shown in Fig. 11.

The magnetic coupler size is 220 mm  $\times$  220 mm  $\times$  10 mm. In the zero- and full-loading conditions, the airgap varying range is from 5 mm to 15 mm. The turn-ratio is an important

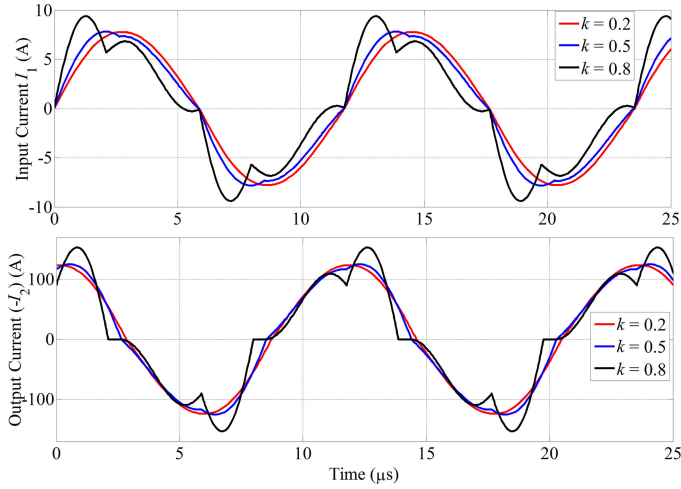


Fig. 10. LTspice-simulated waveforms of  $I_1$  and  $(-I_2)$  at different  $k$  when  $r_I = 1.0$ .

TABLE I

CIRCUIT PARAMETERS OF A 1.8 kW IPT SYSTEM FOR THE AGV CHARGING

| Parameter | Value       | Parameter | Value       |
|-----------|-------------|-----------|-------------|
| $V_{in}$  | 400 V       | $V_{out}$ | 24 V        |
| $f_{sw}$  | 85 kHz      | $k$       | 0.70        |
| $L_1$     | 180 $\mu$ H | $L_2$     | 0.8 $\mu$ H |
| $C_1$     | 19.5 nF     | $C_2$     | 4382.4 nF   |

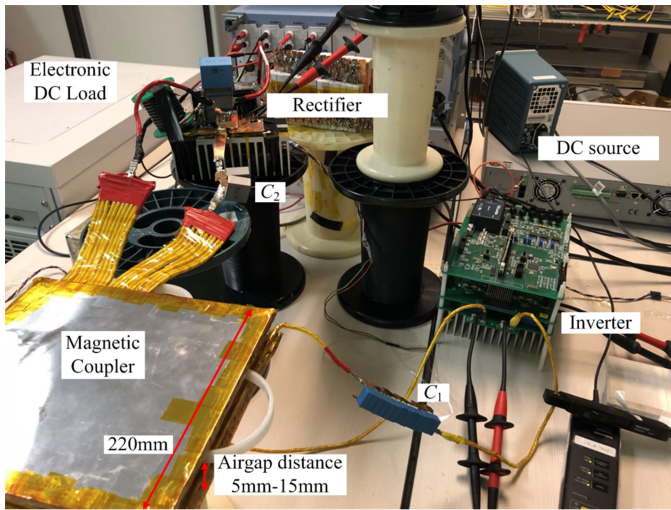


Fig. 11. Prototype of an IPT system for the AGV charging application.

parameter in the coil structure design. The primary coil turn-number is defined as  $N_p$ , and the secondary coil turn-number is defined as  $N_s$ , resulting in the turn-ratio defined as  $N_t = N_p/N_s$ . To achieve the inductances in Table I, for the primary coil, there is  $N_p = 20$ . It is wound by the 600-strand AWG 38 Litz-wire, resulting in a current density of  $1.5 \text{ A/mm}^2$ . For the secondary coil, since  $L_2$  is relatively small and conducts a very high current, there is  $N_s = 1$ , resulting in a turn-ratio  $N_t$  as 20, which is mainly caused by the large difference between the high

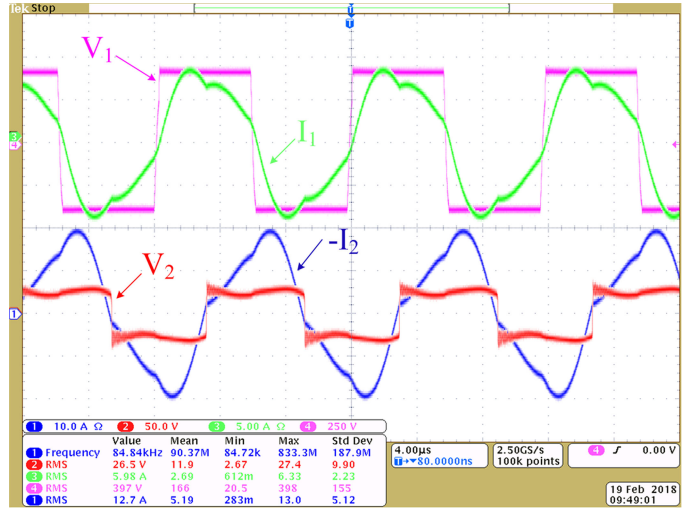


Fig. 12. Experimental waveforms of an AGV system when airgap = 10 mm.

input and low output voltages. In practice,  $L_2$  is wound by ten Litz-wires in parallel to limit its current density to  $2.5 \text{ A/mm}^2$ .

### B. Experimental Results When Airgap = 10 mm

When the input voltage is set to the nominal value 400 V and the output dc voltage is 24 V, the experimental waveforms are shown in Fig. 12. The input and output waveforms are all presented. It validates that both  $I_1$  and  $(-I_2)$  are distorted, which means there are high-order harmonic currents in the system. Due to the range limit of the current probe, only 1/8 of the output current is measured.

Meanwhile, the output power reaches 1.8 kW with a dc-dc efficiency of 89.9% from the dc source to the dc load. The measured output voltage is 24.2 V, and the output current is 74 A, validating a low-voltage and high-current system.

In the experiment, the capacitance  $C_1$  is tuned to 24.5 nF in order to achieve the soft-switching condition for the input-side inverter. Therefore, the switching loss can be eliminated. The silicon carbide (SiC) MOSFETs (C2M0025120D) and low-loss Schottky diodes (DSSK40-008B) are used in the system. At the output side, two diodes are connected in parallel to reduce loss. Then, the loss breakdown is performed based on the datasheets and the quality factor of the passive components. Not including the power losses in the inverter and diode rectifier, the ac-ac efficiency of the resonant circuit is about 95.5%, which validates that the designed tightly-coupled IPT system works in a relatively high-efficiency status.

Most of the power loss (58%) lies in the rectifier. In this low-voltage and high-current scenario, the battery voltage is 24 V, while the charging current is as high as 74 A. According to its datasheet, the voltage drop of each device is only 0.68 V at 40 A forward current. Considering that the typical voltage drop of a silicon P-N junction is about 0.70 V, this device is closed to the optimal option. In future design, to further reduce the power loss in the rectifier, the active synchronous rectifier using low-loss MOSFETs can be adopted at the receiver side.

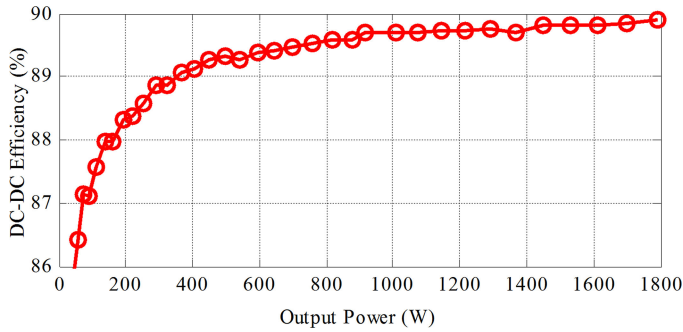


Fig. 13. Experimental output power and dc-dc efficiency when airgap = 10 mm.

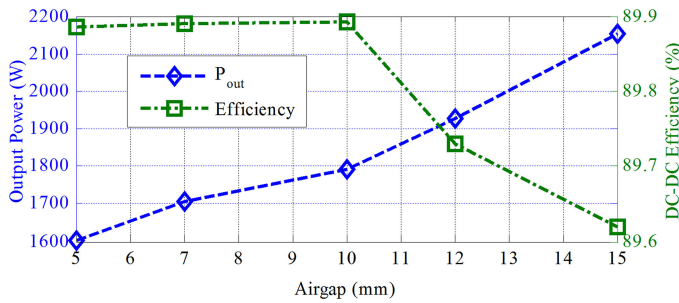


Fig. 14. Experimental power and efficiency when the airgap is from 5 to 15 mm.

When the input voltage increases from a low value to the nominal value (400 V), the system output power and efficiency are measured in Fig. 13, indicating the low load performances. The transfer efficiency increases with the output power. The designed system can maintain a high efficiency over a wide output power range. Particularly, in the low load condition, the system can still maintain a high efficiency. For example, as long as the output power reaches 400 W, the dc-dc efficiency can be higher than 89%. Therefore, the proposed system is suitable for a practical application to charge the AGVs.

### C. Airgap Variation Experiments

Experiments are conducted in different loading conditions and different values of coupling coefficient  $k$ . In the zero- and full-loading conditions of a practical AGV, the airgap distance varies between 5 mm and 15 mm, resulting in a coupling coefficient between 0.60 and 0.75. The experimental results of output power and efficiency are shown in Fig. 14.

Fig. 14 shows that the power variation is within  $\pm 350$  W in the zero- and full-loading conditions, which can be easily compensated by regulating the input voltage. Meanwhile, the efficiency is not significantly affected by the airgap variation, and it varies from 89.6% to 89.9%, which is acceptable for a practical system. When the airgap increases, the slight drop of efficiency is caused by the decreases of coupling coefficient. Considering the high efficiency over a wide working range, the designed SS-compensated IPT system can be used for the AGV charging application.

TABLE II  
FFT ANALYSIS OF THE INPUT CURRENT  $I_1$  AT DIFFERENT AIRGAP DISTANCES

| airgap \ harmonic | 3 <sup>rd</sup> | 5 <sup>th</sup> | 7 <sup>th</sup> | 9 <sup>th</sup> |
|-------------------|-----------------|-----------------|-----------------|-----------------|
| 5 mm              | 37%             | 9.3%            | 7.0%            | 2.8%            |
| 10 mm             | 31%             | 9.1%            | 6.2%            | 3.0%            |
| 15 mm             | 21%             | 8.2%            | 5.1%            | 2.9%            |

Moreover, the FFT analysis of  $I_1$  is conducted as shown in Table II. The third-order harmonic dominates the input current distortion and the other high-order harmonics are small, which validates the circuit analysis in Section II. When the airgap distance is 10 mm, the coupling coefficient is 0.70 and the THD of  $I_1$  is 32%, which agree with the analysis in Fig. 5. When the airgap is 5 mm,  $k$  increases to 0.75 and the THD of  $I_1$  increases to 37%. According to the efficiency analysis in Fig. 7, although the current distortion is visible, the induced power loss by the high-order harmonic currents is not significant. Therefore, the system can maintain a relatively high working efficiency when the airgap distance varies.

In the future research, the other circuit topologies can be studied using the similar method proposed in this paper. For example, the double-sided LCC circuit can help reduce harmonic currents. In a practical application, the compensation inductors can be integrated into the main coil to save space. For given input and output conditions and physical requirements, a comprehensive methodology can be developed to provide the guideline for system design. To sum up, more research work will be continued to further improve the performance of the AGV charging system.

## IV. CONCLUSION

This paper proposes an SS compensation circuit to realize a low-voltage and high-current IPT system for the AGV charging application. The circuit working principle and efficiency are analyzed at different coupling coefficient and circuit parameter combinations. This paper made three main contributions. First, the problem of the high-order harmonic currents is discovered in a tightly-coupled IPT system. Second, it is shown that the harmonic currents can reduce the system efficiency. Third, this paper proposes a circuit design method to reduce the harmonic currents and maintain the system efficiency. A low-voltage and high-current IPT system is implemented. It achieves 1.8 kW power transfer with a dc-dc efficiency of 89.9% from a 400 V dc source to a 24 V battery load. When the airgap varies between 5 mm to 15 mm, the output power variation is within  $\pm 350$  W and the transfer efficiency is not significantly influenced.

## REFERENCES

- [1] G. A. Covic and J. T. Boys, "Inductive power transfer," *Proc. IEEE*, vol. 101, no. 6, pp. 1276–1289, Jun. 2013.
- [2] S. Li and C. Mi, "Wireless power transfer for electric vehicle applications," *IEEE J. Emerging Sel. Top. Power Electron.*, vol. 3, no. 1, pp. 4–17, Mar. 2015.
- [3] A. Foote and O. C. Onar, "A review of high-power wireless power transfer," in *Proc. IEEE Transp. Electrific. Conf. Expo.*, 2017, pp. 234–240.

- [4] Z. Huang, S. C. Wong, and C. K. Tse, "Design of a single-stage inductive-power-transfer converter for efficient EV battery charging," *IEEE Trans. Veh. Technol.*, vol. 66, no. 7, pp. 5808–5821, Jul. 2017.
- [5] F. Lu, H. Zhang, H. Hofmann, W. Su, and C. Mi, "A dual-coupled LCC-compensated IPT system with a compact magnetic coupler," *IEEE Trans. Power Electron.*, vol. 33, no. 7, pp. 6391–6402, Jul. 2018.
- [6] X. Dai, X. Li, Y. Li, and A. P. Hu, "Impedance matching range extension method for maximum power transfer tracking in IPT system," *IEEE Trans. Power Electron.*, vol. 33, no. 5, pp. 4419–4428, May 2018.
- [7] W. Zhang, S. C. Wong, K. T. Chi, and Q. Chen, "Design for efficiency optimization and voltage controllability of series-series compensated inductive power transfer systems," *IEEE Trans. Power Electron.*, vol. 29, no. 1, pp. 191–200, Jan. 2014.
- [8] Y. Sohn, B. Choi, E. Lee, G. Lim, G. Cho, and C. T. Rim, "General unified analyses of two-capacitor inductive power transfer systems: Equivalence of current-source SS and SP compensations," *IEEE Trans. Power Electron.*, vol. 30, no. 11, pp. 6030–6045, Nov. 2015.
- [9] N. Rasekh, J. Kavianpour, and M. Mirsalim, "A novel integration method for a bipolar receiver pad using LCC compensation topology for wireless power transfer," *IEEE Trans. Veh. Technol.*, vol. 67, no. 8, pp. 7419–7428, Aug. 2018.
- [10] X. T. Garcia, J. Vazquez, and P. Roncero-Sanchez, "Design, implementation issues, and performance of an inductive power transfer system for electric vehicle chargers with series-series compensation," *IET Power Electron.*, vol. 8, no. 10, pp. 1920–1930, Oct. 2015.
- [11] B. Esteban, M. Sid-Ahmed, and N. C. Kar, "A comparative study of power supply architectures in wireless EV charging systems," *IEEE Trans. Power Electron.*, vol. 30, no. 11, pp. 6408–6422, Nov. 2015.
- [12] J. Lu, G. Zhu, D. Lin, S. C. Wong, and J. Jiang, "Load-independent voltage and current transfer characteristic of high-order resonant network in IPT system," *IEEE J. Emerging Sel. Top. Power Electron.*, vol. 7, no. 1, pp. 6408–6422, Mar. 2019.
- [13] W. Zhang, S. C. Wong, C. K. Tse, and Q. Chen, "Load-independent duality of current and voltage outputs of a series- or parallel-compensated inductive power transfer converter with optimized efficiency," *IEEE J. Emerging Sel. Top. Power Electron.*, vol. 3, no. 1, pp. 137–146, Mar. 2015.
- [14] J. Yin, D. Lin, T. Parisini, and S. Y. Hui, "Front-end monitoring of the mutual inductance and load resistance in a series-series compensated wireless power transfer system," *IEEE Trans. Power Electron.*, vol. 31, no. 10, pp. 7339–7352, Oct. 2016.
- [15] W. Zhang, S. C. Wong, C. K. Tse, and Q. Chen, "Analysis and comparison of secondary series- and parallel-compensated inductive power transfer systems operating for optimal efficiency and load-independent voltage-transfer Ratio," *IEEE Trans. Power Electron.*, vol. 29, no. 6, pp. 2979–2990, Jun. 2014.
- [16] S. Hasanzadeh, S. Vaez-Zadeh, and A. H. Isfahani, "Optimization of a contactless power transfer system for electric vehicles," *IEEE Trans. Veh. Technol.*, vol. 61, no. 8, pp. 3566–3573, Oct. 2012.
- [17] S. Wang, J. Chen, Z. Hu, C. Rong, and M. Liu, "Optimization design for series-series dynamic WPT system maintaining stable transfer power," *IET Power Electron.*, vol. 10, no. 9, pp. 987–995, Jul. 2017.
- [18] J. Hou, Q. Chen, S. C. Wong, C. K. Tse, and X. Ruan, "Analysis and control of series-series-parallel compensated resonant converter for contactless power transfer," *IEEE J. Emerging Sel. Top. Power Electron.*, vol. 3, no. 1, pp. 124–136, Mar. 2015.
- [19] I. I. Nam, R. A. Gougal, and E. Santi, "Novel unity-gain frequency tracking control of series-series resonant converter to improve efficiency and receiver positioning flexibility in wireless charging of portable electronics," *IEEE Trans. Ind. Appl.*, vol. 51, no. 1, pp. 385–297, Jan./Feb. 2015.
- [20] S. Samanta, A. K. Rathore, and D. J. Thrimawithana, "Bidirectional current-fed half-bridge (C) (LC)-(LC) configuration for inductive wireless power transfer system," *IEEE Trans. Ind. Appl.*, vol. 53, no. 4, pp. 4053–4062, Jul./Aug. 2017.
- [21] E. Fatnassi and J. Chaouachi, "Scheduling automated guided vehicle with battery constraints," in *Proc. Conf. Method Model Auto. Robot.*, 2015, pp. 1010–1015.
- [22] T. Mercy, R. V. Parys, and G. Pipeleers, "Spline-based motion planning for autonomous guided vehicles in a dynamic environment," *IEEE Trans. Control Syst. Technol.*, vol. 26, no. 6, pp. 2182–2189, Nov. 2018.
- [23] M. Kissin, H. Hao, and G. A. Covic, "A practical multiphase IPT system for AGV and roadway applications," in *Proc. IEEE Energy Convers. Cong. Expo.*, 2010, pp. 1844–1850.
- [24] J. Zhang, C. Zhu, and C. C. Chan, "A wireless power charging method for Automated Guided Vehicle," in *Proc. IEEE Int. Elect. Veh. Conf.*, 2014, pp. 1–5.
- [25] S. Huang, S. Dai, J. Su, and T. Lee, "Design of a contactless power supply system with dual output capability for AGV applications," in *Proc. IEEE Global Conf. Consum. Electron.*, 2017, pp. 1–3.
- [26] A. Ecklebe and A. Lindemann, "Analysis and design of a contactless energy transmission system with flexible inductor positioning for automated guided vehicles," in *Proc. IEEE Conf. Ind. Electron.*, 2006, pp. 1721–1726.
- [27] J. Deng, S. Li, S. Hu, C. Mi, and R. Ma, "Design methodology of LLC resonant converters for electric vehicle battery chargers," *IEEE Trans. Veh. Technol.*, vol. 63, no. 4, pp. 1581–1592, May 2014.
- [28] X. Zhang, T. Kan, C. You, and C. Mi, "Modeling and analysis of AC output power factor for wireless chargers in electric vehicles," *IEEE Trans. Power Electron.*, vol. 32, no. 2, pp. 1481–1492, Feb. 2017.
- [29] B. Pang, J. Deng, P. Liu, and Z. Wang, "Secondary-side power control method for double-side LCC compensation topology in wireless EV charger application," in *Proc. IEEE Ind. Electron. Conf.*, 2017, pp. 7860–7865.
- [30] C. Xia, R. Chen, Y. Liu, L. Liu, and G. Chen, "Inhibition of current harmonics in LCL/LCC wireless power transfer system," in *Proc. IEEE Workshop Emerging Technol. Wireless Power Trans.*, 2017, pp. 1–6.
- [31] H. R. Rahnamaee, U. K. Madawala, and D. J. Thrimawithana, "Minimizing total harmonic distortion in a multi-level based WPT system," in *Proc. IEEE Sothern Power Electron. Conf.*, 2017, pp. 1–6.
- [32] H. Kim, S. Jeong, D. Kim, J. Kim, Y. Kim, and I. Kim, "Selective harmonic elimination method of radiation noise from automotive wireless power transfer system using active rectifier," in *Proc. IEEE Elect. Perform. Electron. Packag. Syst.*, 2016, pp. 161–164.
- [33] A. Moradi, F. Tahami, and M. A. GhaziMoghadam, "Wireless power transfer using selected harmonic resonance mode," *IEEE Trans. Transp. Electrific.*, vol. 3, no. 2, pp. 508–519, Jun. 2017.
- [34] M. Liu, M. Fu, and C. Ma, "Low-harmonic-contents and high-efficiency class e full-wave current-driven rectifier for megahertz wireless power transfer systems," *IEEE Trans. Power Electron.*, vol. 32, no. 2, pp. 1198–1209, Feb. 2017.
- [35] H. Zeng, S. Yang, and F. Z. Peng, "Design consideration and comparison of wireless power transfer via harmonic current for PHEV and EV wireless charging," *IEEE Trans. Power Electron.*, vol. 32, no. 8, pp. 5943–5952, Aug. 2017.
- [36] H. Zeng, N. S. Santini, Y. Yu, S. Yang, F. Z. Peng, "Harmonic burst control strategy for full-bridge series-resonant converter-based EV charging," *IEEE Trans. Power Electron.*, vol. 32, no. 5, pp. 4064–4073, May 2017.
- [37] H. Zhang, Y. Guo, S. Guo, and W. Wu, "Wireless power transfer antenna alignment using third harmonic," *IEEE Microw. Wireless Comp. Lett.*, vol. 28, no. 6, pp. 536–538, Jun. 2018.
- [38] Z. Pantic, K. Lee, and S. M. Lukic, "Receivers for multifrequency wireless power transfer: Design for minimum interference," *IEEE J. Emerging Sel. Top. Power Electron.*, vol. 3, no. 1, pp. 234–241, Mar. 2015.
- [39] W. X. Zhong and S. Y. R. Hui, "Maximum energy efficiency tracking for wireless power transfer systems," *IEEE Trans. Power Electron.*, vol. 30, no. 7, pp. 4025–4034, Jul. 2015.
- [40] H. Li *et al.*, "A maximum efficiency point tracking control scheme for wireless power transfer systems using magnetic resonant coupling," *IEEE Trans. Power Electron.*, vol. 30, no. 7, pp. 3998–4008, Jul. 2015.
- [41] C. P. Steinmetz, "On the law of hysteresis," *Proc. IEEE*, vol. 72, no. 2, pp. 196–212, Apr. 1984.



**Fei Lu** (S'12–M'17) received the B.S. and M.S. degrees from the Harbin Institute of Technology, Harbin, China, in 2010 and 2012, respectively, and the PhD degree from the University of Michigan, Ann Arbor, MI, USA, in 2017, all in electrical engineering.

He is currently an Assistant Professor with the Department of Electrical and Computer Engineering in Drexel University, Philadelphia, PA, USA. His research interests focus on power electronics and the application of electric vehicle charging.



**Yiming Zhang** (S'13–M'16) received the B.S. and Ph.D. degrees in electrical engineering from Tsinghua University, Beijing, China, in 2011 and 2016, respectively.

He is currently a Postdoctoral Researcher with San Diego State University, San Diego, CA, USA. His research interests include wireless power transfer for electric vehicles and mobile phones, and resonant converters.



**Minming Gong** received the B.Eng. and M.Eng. degrees in electrical engineering from Beijing Jiaotong University, Beijing, China, in 1994 and 2008, respectively.

He is currently a Senior Engineer with the School of Electrical Engineering, Beijing Jiaotong University, and a Vice-Dean of National Active Distribution Network Technology Research Center. His research interests include lithium battery group technology and new energy.



**Hua Zhang** (S'14–M'17) received the B.S., M.S., and Ph.D. degrees in electrical engineering from Northwestern Polytechnical University, Xi'an, China, in 2011, 2014, and 2017, respectively.

From September 2014 to August 2015, she was a joint Ph.D. student funded by the China Scholarship Council with the University of Michigan, Dearborn. From September 2015, she started to work in San Diego State University. She is currently a Postdoctoral Research Associate with Drexel University, Philadelphia, PA, USA. Her research interests include charging of electric vehicles.



**Chong Zhu** (M'17) received the B.S. degree in electrical engineering from the China University of Mining and Technology, Xuzhou, China, in 2010, and the Ph.D. degree in electrical engineering from Zhejiang University, Hangzhou, China, in 2016.

He is currently a Postdoctoral Researcher with San Diego State University, San Diego, California, USA. His research interests include battery thermal management, AC/DC power conversion, and pulsewidth modulation techniques applied in EVs.



**Weige Zhang** received the M.S. and Ph.D. degrees in electrical engineering from Beijing Jiaotong University, Beijing, China, in 1997 and 2013, respectively.

He is currently a Professor with the School of Electrical Engineering, Beijing Jiaotong University. His research interests include battery pack application technology, power electronics, and intelligent distribution system.



**Lijun Diao** (M'10–SM18') received the B.Eng. and Ph.D. degrees in electrical engineering from Beijing Jiaotong University, Beijing, China, in 2003 and 2008, respectively.

He is currently a Vice-Dean of Beijing Engineering Research Center for Electrical Rail Transit. He was PI of the traction systems' R&D for China's first 100% low floor light rail vehicle and first hybrid EMU. His research interests include power electronics and ac drives, transportation and ship electrification applications, hybrid energy management, safety control, etc.



**Chunting Chris Mi** (S'00–A'01–M'01–SM'03–F'12) received the B.S.E.E. and M.S.E.E. degrees in electrical engineering from Northwestern Polytechnical University, Xi'an, China, and the Ph.D. degree in electrical engineering from the University of Toronto, Toronto, Ontario, Canada, in 1985, 1988, and 2001, respectively.

He is a Professor and Chair of electrical and computer engineering and the Director of the Department of Energy funded Graduate Automotive Technology Education Center for Electric Drive Transportation, San Diego State University (SDSU), San Diego, USA. Prior to joining SDSU, he was with the University of Michigan, Dearborn from 2001 to 2015.